Amorphous Zirconia-doped Tantala modeling and simulations using explicit multi-element spectral neighbor analysis machine learning potentials (EME-SNAP)

Jun Jiang [1,*] Xiang-Guo Li [2] Alec S. Mishkin [1] Rui Zhang [1] Riccardo Bassiri [3] James N. Fry [1] Martin M. Fejer [3] and Hai-Ping Cheng [1,†]

[1]*Department of Physics, The Quantum Theory Project, University of Florida, Gainesville, Florida 32611, USA*
[2]*School of Materials, Sun Yat-sen University, Shenzhen, Guangdong 518107, China*
[3]*E. L. Ginzton Laboratory, Stanford University, Stanford, California 94305, USA*

(Received 26 January 2022; accepted 31 March 2023; published 20 April 2023)

We model amorphous Zirconia-doped Tantala with machine learning interactomc potentials based on explicit multielement spectral neighbor analysis (EME-SNAP). These atomic structure models can reproduce partial radial distribution functions obtained from first-principles calculations and elastic moduli found from experimental measurements. The two-body pair forces calculated from EME-SNAP further affirm that the potentials capture the atomic interactions well. Molecular dynamics simulations of simulated annealing with EME-SNAP show that the final density of the amorphous models depends on the thermal history even when the annealing rate is kept constant, which captures experimental observations of history-dependent densities. Mechanical spectroscopy is also simulated using both Morse-Beest-Kramer-Santen pair potentials and EME-SNAP. The success in applying the EME-SNAP to amorphous Zirconia-doped Tantala pushes the boundaries of simulation accuracy and system size and enables better and more realistic atomistic modeling for amorphous systems. There are still some limitations in applying the potentials generated in this paper. They are only optimized for trained amorphous phases; high-temperature stability and transferability need to be further investigated.

DOI: 10.1103/PhysRevMaterials.7.045602

I. INTRODUCTION

Tantala (Ta_2O_5) is an important material in the semiconductor industry where it can serve as a barrier layer due to its sufficient band gap. With a high refractive index and low optical absorption, amorphous tantala is used in dielectric mirrors, such as those in the laser interferometer gravitational-wave observatory (LIGO), alternating with thin layers of silica (SiO_2) [1,2]. Thermal annealing at a higher temperature can reduce both optical and mechanical losses, the latter important for reducing thermal noise in precision measurement applications, such as LIGO. Zirconia also has a high refractive index, and recent experiments show that zirconia can frustrate crystallization in tantala thin films, allowing for annealing at much higher temperatures without crystallization [3]. To better understand the doping effects, modeling and simulations are essential to obtain the underlying atomic structures.

Atomic structures of amorphous materials depend on their deposition methods and thermal history [3–6], which makes it very difficult to generate proper structure models even with the physical constraints from experimental measurements, such as density and radial distribution functions (RDFs). Various approaches, such as melting and quenching, simulated annealing, reverse Monte Carlo, etc., have been used to build realistic models. By combining experimental RDFs with the reverse Monte Carlo (RMC) method and forces from calculations, force-enhanced atomic refinement has been shown to produce realistic atomic models of amorphous materials [7].

Doping introduces additional challenges to the modeling process as more element types will create more complex atomic structures. Also, different elements have different interactions. Unified interatomic potentials [8–10] have been developed to account for this. By simply mixing potentials from pure oxides of the same form with effective Coulomb interactions between different metal atoms, complex doping systems can be described with the combined potentials. Beest-Kramer-Santen (BKS) potentials were initially invented for silica (SiO_2) and aluminophosphate [8]. Zirconia (ZrO_2) BKS potentials have also been developed and combined with the silica BKS potential to enable the study of energy recoil damage in $ZrSiO_4$. The thermal expansion, relative stability and phase-transition properties calculated with these potentials are consistent with experimental and density functional theory (DFT) results [9]. By adding a Morse term to the BKS potential, amorphous SiO_2, ZrO_2, Ta_2O_5, TiO_2 and HfO_2 are unified into Morse-BKS potential form, and models based on Morse-BKS potentials give RDFs that agree with DFT models generated from experimental results [10]. With these potentials the optimal TiO_2-doping concentration for amorphous Ta_2O_5 that produces the lowest mechanical loss from molecular dynamics modeling is consistent with the experimental measurements [11]. By combining classical pair potentials with the reverse Monte Carlo RMC method to fit to experimental x-ray grazing-incidence pair distribution function (GIPDF) data, it has been shown that annealing reduces

*jiangjun413@ufl.edu
†hping@ufl.edu

the percentage of face-sharing and edge-sharing polyhedra in ZrO_2-doped Ta_2O_5 [12], which led to the discovery of TiO_2-doped GeO_2 with superior mechanical loss performance for LIGO mirror coatings [13]. Morse-BKS potentials have also been used to identify two different types of two-level system transitions in amorphous ZrO_2-doped Ta_2O_5, denoted non-cage-breaking and cage-breaking transitions, which contribute to the loss peaks at different temperatures [14]. In pure Ta_2O_5 the *in silico* broadband mechanical spectroscopy method, using the Morse-BKS potentials the calculated mechanical loss matches experimental measurements closely at low temperatures [15].

Despite these successful applications of the RMC method and unified Morse-BKS potential for amorphous-doped oxides mentioned above, there are still some problems that remain to be solved. For example, the metal-metal interactions are not accurate. In ZrO_2-doped Ta_2O_5, the Ta-Ta and Ta-Zr partial RDFs show much lower strength at the first metal-metal peak compared to experimental and DFT results. The energies calculated from Morse-BKS potentials do not agree with the DFT-calculated energies. With exactly the same set of atomic structures, the potential-energy differences between any two of them computed with DFT are about three times larger than those computed with Morse-BKS potentials. The Morse-BKS potential form is not fit for some amorphous oxides, such as amorphous germanium dioxide whose BKS potential gives longer Ge-Ge distances compared to experimental observations [16–20].

Compared to the force field approach, simulations based on DFT calculations can be quite accurate for these complex systems, but the size of the models is limited due to the relatively high calculation cost, which increases rapidly with the number of atoms. For amorphous modeling, simulation boxes containing more than a few hundred atoms for pure systems and a few thousand of atoms for doped systems are needed to give statistically meaningful results from averaging over all possible atomic environments for which DFT calculations are prohibitively expensive.

In this paper, we generate an explicit multielement spectral neighbor analysis potential (EME-SNAP) for amorphous Zirconia-doped Tantala to enable the modeling of amorphous materials more accurately than the Morse-BKS potentials and faster than DFT calculations. The SNAP has a general form, which can potentially be applied to different oxides and doped systems.

II. METHOD

A. Bispectrum and SNAP formalism

Simulations using machine-learned potentials start from abstracted features to calculate material properties, such as energy and force. In this paper, the SNAP is used, which utilizes bispectrum components as features to characterize the local neighborhood of each atom and linear regression to fit to targeted properties. The bispectrum was initially used in Gaussian approximation potentials and proved to have accuracy comparable to quantum mechanics in calculating the potential-energy surface without the electrons [21–23]. Instead of the original weighted density (WD) SNAP [24,25], the EME-SNAP [26] is used due to its improved chemical sensitivity, which is achieved by separating the contributions from different elements with partial atomic densities.

To calculate the explicit multielement bispectrum components, the partial atomic neighbor density for element μ at position $\boldsymbol{r}$ is defined as

$$\rho^{\mu}(\boldsymbol{r}) = w^{\text{self}}_{\mu_i\mu}\delta(0) + \sum_{r_{ik}<R^{\mu_i\mu_k}_{\text{cut}}} \delta_{\mu\mu_k} f_c\left(r_{ik}; R^{\mu_i\mu}_{\text{cut}}\right) w_{\mu_k}\delta(r_{ik}), \quad (1)$$

where r_{ik} is the position of neighbor atom k relative to central atom i, and w_{μ} is a dimensionless weight to discriminate atom types. The cutoff function f_c ensures that the neighbor atomic density decreases smoothly to zero at the cutoff radius $R^{\mu_i\mu_k}_{\text{cut}}$. Only the element μ contributes to the partial density ρ^{μ}.

The radial distribution is converted into an additional polar angle θ_0 defined by $\theta_0 = r_{ik}\,\theta_0^{\max}/R^{\mu_i\mu_k}_{\text{cut}}$. Thus, the density function can be represented in three-spherical coordinates (θ_0, θ, ϕ) coordinates instead of (r, θ, ϕ), and the density function on the three-sphere can be expanded with four-dimensional hyperspherical harmonics $\boldsymbol{U}_j(\theta_0, \theta, \phi)$ as

$$\rho^{\mu}(\boldsymbol{r}) = \sum_{j=0,1/2,\ldots}^{\infty} \boldsymbol{u}^{\mu}_j \cdot \boldsymbol{U}_j(\theta_0, \theta, \phi), \quad (2)$$

where the coefficients $\boldsymbol{u}^{\mu}_j$ are obtained as the inner product of the neighbor density functions with the basis function given by

$$\boldsymbol{u}^{\mu}_j = w^{\text{self}}_{\mu_i\mu}\boldsymbol{U}_j(0) + \sum_{r_{ik}<R^{\mu_i\mu_k}_{\text{cut}}} \delta_{\mu\mu_k} f_c\left(r_{ik}; R^{\mu_i\mu}_{\text{cut}}\right) w_{\mu_k}\boldsymbol{U}_j(\theta_0, \theta, \phi). \quad (3)$$

The bispectrum components $B_{j_1j_2j}$ can then be obtained via

$$B_{j_1j_2j} = \sum_{\kappa,\lambda,\mu=1}^{N_{\text{elem}}} B^{\kappa\lambda\mu}_{j_1j_2j}, \quad (4)$$

$$B^{\kappa\lambda\mu}_{j_1j_2j} = \frac{1}{2j+1}\boldsymbol{u}^{\kappa}_{j_1} \bigotimes_{j_1j_2j} \boldsymbol{u}^{\lambda}_{j_2} \cdot \left(\boldsymbol{u}^{\mu}_j\right)^*, \quad (5)$$

where $\bigotimes_{j_1j_2j}$ represents the Clebsch-Gordan product of matrices of degrees j_1 and j_2 that produces a matrix of degree j defined in the original SNAP formulation [24]; j must satisfy the conditions $\|j_1 - j_2\| \leqslant j \leqslant \|j_1 + j_2\|$.

In EME-SNAP, the total energy $E(\boldsymbol{r}^N)$ and forces $\boldsymbol{F}_k$ are expressed as linear functions of projected bispectrum components $\boldsymbol{B}_i$ and their derivatives,

$$E(\boldsymbol{r}^N) = \sum_{\mu=1}^{N_{\text{elem}}} \boldsymbol{\beta}_{\mu} \cdot \sum_{i=1}^{N} \boldsymbol{B}_i, \quad (6)$$

$$\boldsymbol{F}_k = -\sum_{\mu=1}^{N_{\text{elem}}} \boldsymbol{\beta}_{\mu} \cdot \sum_{i=1}^{N} \frac{\partial \boldsymbol{B}_i}{\partial \boldsymbol{r}_k}, \quad (7)$$

where $\boldsymbol{B}_i$'s are the $(N_B N^3_{\text{elem}})$ EME bispectrum components for atom i and the $\boldsymbol{\beta}_{\mu}$ are the $(N_B N^3_{\text{elem}})$ coefficients fitted from the training process.

B. Training structures and parameters optimization

In this section, we generate an EME-SNAP machine learning potential for amorphous Zirconia-doped Tantala that includes three elements (Ta, Zr, and O) explicitly.

The first step in constructing a potential is to prepare the training set. In addition to the crystalline zirconia and crystalline tantala models, amorphous zirconia, amorphous tantala, and amorphous Zirconia-doped Tantala models are also used as training structures. The crystalline models are experimentally verified phases from The Materials Project [27]. The amorphous models are made from melting-quenching crystal structures using classical pair potentials or DFT calculations. Each model produces a series of training structures by randomly shifting atoms, distorting cells and creating molecular dynamics (MD) trajectories. The energies, forces and stresses of these models from DFT calculations are used as the training set. The comparison between experimental elastic moduli and calculated ones is discussed in Sec. III D.

MD simulations based on classical pair potentials and SNAP potentials are performed using the large-scale atomic/molecular massively parallel simulator (LAMMPS) software package [28]. The BKS pair potential [9] for zirconia and the Morse-BKS potential [10] for tantala are used as the classical pair potentials. First-principles calculations are performed using the Vienna *ab initio* simulation program code [29–31] derived from self-consistent DFT [32] using projector-augmented wave potentials [33,34] in conjunction with the plane-wave expansion. The exchange and correlation functional are calculated using the parameter-free generalized gradient approximation developed by Perdew, Burke, and Ernzerhof [35]. The energy cutoff is 520 eV. For crystal structures the k mesh is $7 \times 7 \times 7$ or $11 \times 11 \times 11$ using the Monkhorst-Pack scheme [36] depending on the unit-cell size. For amorphous structures, only the Γ point is considered in the calculations. The energy and force convergence criteria are 10^{-6} eV and 0.02 eV/Å, respectively.

Once we have the training set, the bispectrum coefficients are calculated using the LAMMPS [28] software package developed by Thompson [24]. The training of the SNAP potentials is performed using the python package FITSNAP [37]. The hyperparameters and cutoffs of atoms are optimized through grid searching. The cutoff radius for Ta is 3.43 Å, for O is 2.45 Å, and for Zr is 3.67 Å. The weights of Ta, O, and Zr are 0.92, 1.00, and 0.67.

III. SNAP POTENTIAL RESULTS AND APPLICATIONS

A. Training errors of energies, forces, and stresses

The training structures for crystal Ta_2O_5 are mp-10390, mp-554867, and mp-624688. For crystalline ZrO_2, mp-1190186, mp-1565, mp-2574, mp-2858, mp-556605, and mp-963 are used. (IDs are indexed in materials project database [27]) The crystal structures are only primitive cells. The shifted, distorted, and MD trajectories of the crystal phases are starting from crystalline supercells, which are 300–1000 atoms, and the supercells are enlarged to be as cubic in shape as possible.

The reference energies, forces, and stresses (DFT) and predicted energies, forces, and stresses (SNAP) from the training set (randomly selected in all models) are plotted in Figs. 1(a), 1(c) and 1(e), respectively. The testing set (randomly selected from all models besides the training models) error distributions are shown in Figs. 1(b), 1(d) and 1(f). These results demonstrate that the energies and forces from SNAP are in agreement with the DFT references. The total mean absolute errors (MAEs) are 1.5 meV per atom for energy and 0.22 eV/Å for force. The MAEs of energies and forces for each type of training set are shown in Table I. The force stress tensors of each model calculated from SNAP also match the DFT references reasonably well, even though they are not training properties. Both the training and the testing errors show almost the same error distribution and no overfitting is found during training tests with different training set sizes.

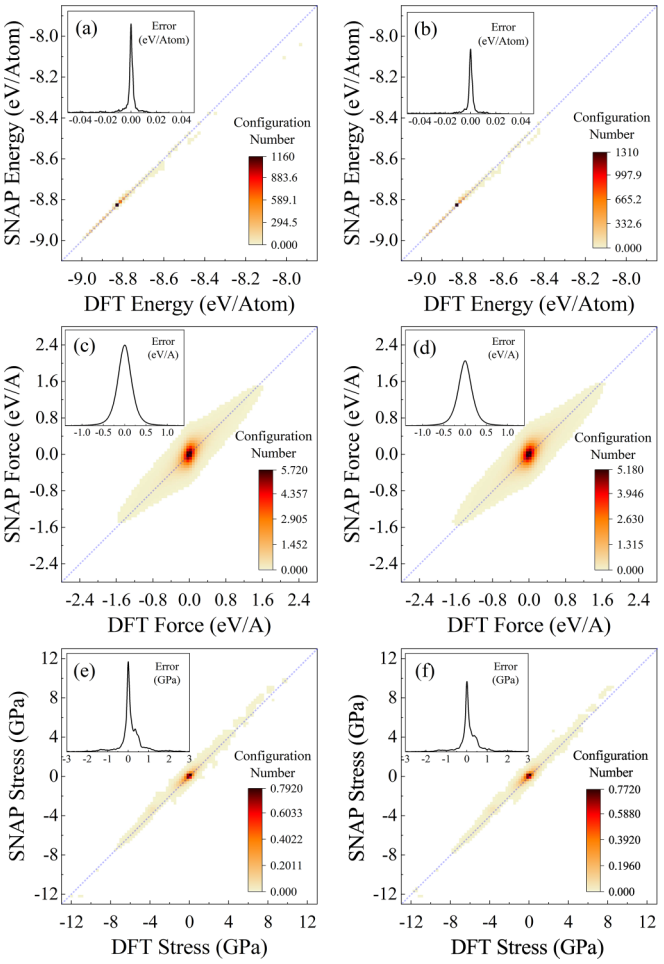

FIG. 1. The distribution of training and testing errors for energies, forces, and stresses when EME-SNAP results are compared to DFT references.

B. Two-body pair force comparison

Unlike the simple form of the classical two-body pair potential, the EME-SNAP has hundreds of parameters and includes many-body interactions. Besides comparing energies, forces and stresses to first-principle calculations, it is necessary to check two-body interactions and see how well the EME-SNAP works in this limit. Here, we performed force calculations between various pairs in the system to give in-

TABLE I. The MAEs of energies and forces for each type of training set.

Type	N_{config}	N_{force}	E_{MAE} (eV/atom)	F_{MAE} (eV/Å)
Crystalline Ta_2O_5	860	2.7×10^4	1.2×10^{-3}	1.5×10^{-1}
Crystalline ZrO_2	2104	9.2×10^4	8.2×10^{-4}	6.5×10^{-2}
Liquid O_2	37	7.1×10^4	2.1×10^{-3}	2.9×10^{-1}
Amorphous Ta_2O_5	261	5.7×10^5	8.7×10^{-4}	1.8×10^{-1}
Amorphous ZrO_2	540	1.1×10^6	7.3×10^{-4}	1.1×10^{-1}
12% ZrO_2-doped Ta_2O_5	48	1.4×10^5	7.5×10^{-4}	2.1×10^{-1}
25% ZrO_2-doped Ta_2O_5	56	1.6×10^5	9.0×10^{-4}	2.1×10^{-1}
38% ZrO_2-doped Ta_2O_5	69	2.0×10^5	6.7×10^{-4}	2.1×10^{-1}
50% ZrO_2-doped Ta_2O_5	1143	3.0×10^6	2.9×10^{-4}	2.9×10^{-1}
50% ZrO_2-doped Ta_2O_5 small	3926	3.3×10^6	3.0×10^{-3}	3.3×10^{-1}

sight into the EME-SNAP. With only two atoms included the forces are calculated by continually changing the distance between the two atoms. There are six types of pairs: Ta-O, Zr-O, O-O, Ta-Ta, Zr-Zr, and Ta-Zr. The two-body pair forces of each type are shown in Fig. 2. The forces shown are calculated based on self-consistent DFT, the Morse-BKS pair potentials, and the EME-SNAP for comparison.

From these results, we find that the EME-SNAP two-body pair forces for Ta-O and Zr-O are similar to the forces derived from the Morse-BKS potentials, which are almost on top of the DFT results below 3.5 Å. All sets of forces have a minimum near 2.0 Å for Ta-O and 2.1 Å for Zr-O with similar magnitudes. In amorphous oxides, the metal atoms are mostly surrounded by oxygen atoms, which makes the metal-oxygen "bonds" one of the most important interactions. From previous studies [8–10], the analytic form of the Morse-BKS potential comes from physical understanding and has proven to be very successful in modeling amorphous oxides, such as Ta_2O_5 and ZrO_2. On the other hand, the EME-SNAP is only trained from the energies, forces and stresses from first-principle calculations, and, thus, there is no physical understanding, such as bonds or effective charges included. The similarity in the two-body pair forces of Ta-O and Zr-O from DFT, Morse-BKS, and EME-SNAP is solid evidence that both the Morse-BKS potential and the EME-SNAP have captured the physical interactions between metal and oxygen atoms in amorphous ZrO_2-doped Ta_2O_5 . These metal-oxygen interactions are directly related to the short-range order of the RDF in amorphous oxides, and indeed the RDFs in the following section affirm that both potentials agree on the short-range order.

The two-body pair forces of O-O from the Morse-BKS potential are always repulsive, whereas O-O from EME-SNAP shows bonding behavior near 1.4 Å, similar to DFT, which

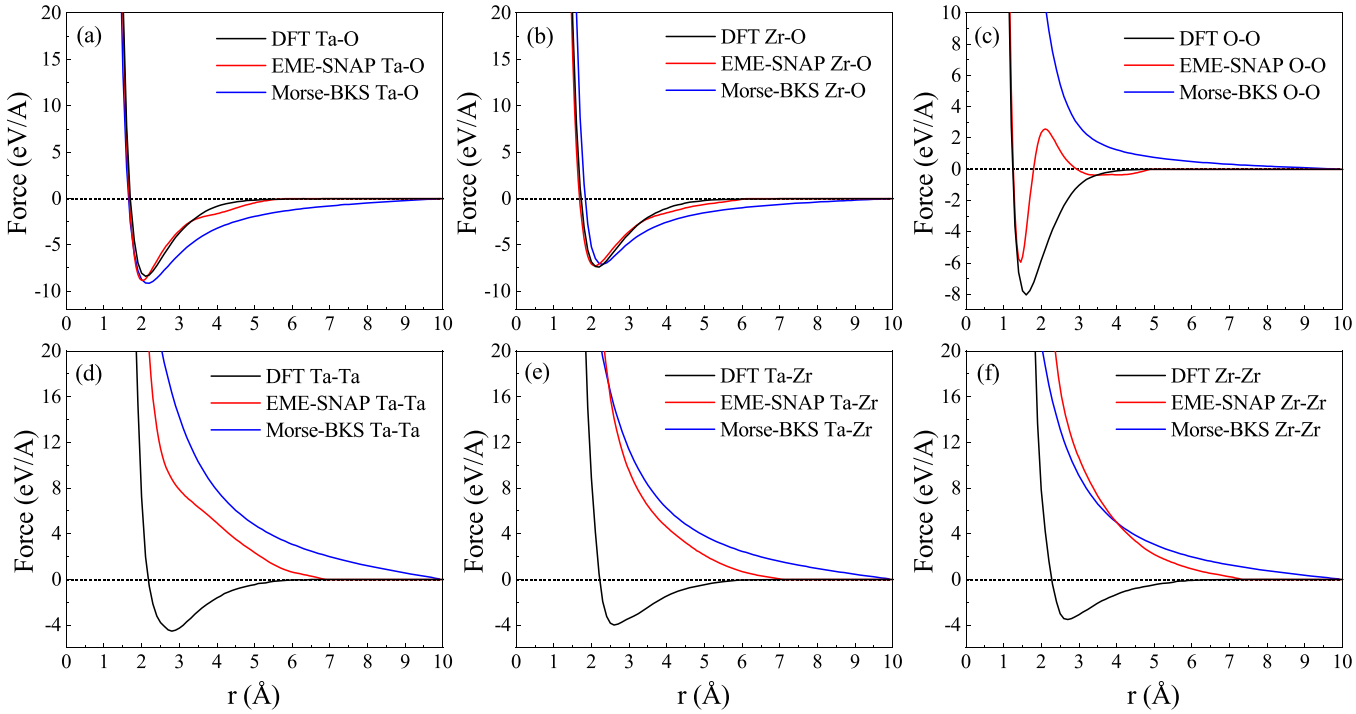

FIG. 2. Two-body pair force comparison among the DFT (black), the EME-SNAP potential (red), and the Morse-BKS potential (blue) for (a) Ta-O, (b) Zr-O, (c) O-O, (d) Ta-Ta, (e) Ta-Zr, and (f) Zr-Zr in amorphous ZrO_2-doped Ta_2O_5.

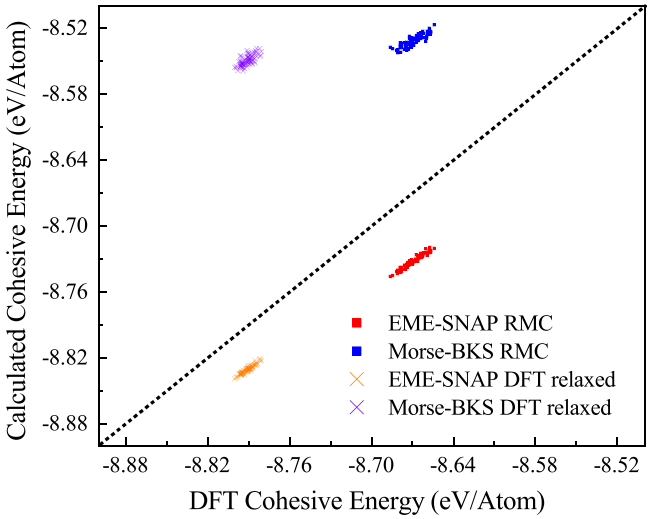

FIG. 3. Cohesive energies of RMC- and DFT-relaxed models (50% ZrO_2-doped Ta_2O_5 with 975 atoms) from DFT, the Morse-BKS potential and EME-SNAP. The horizontal axis is the cohesive energy from DFT and the vertical axis is the calculated cohersive energy from Morse-BKS or EME-SNAP. The black dotted line is for reference where the calculated energy match the DFT energy. The square symbols are RMC models and the cross symbols are models whose atomic structures are relaxed by minimizing their DFT energies.

makes the EME-SNAP more correct physically when considering only O-O interactions. For the Morse-BKS potentials, Ta-Ta, Ta-Zr, and Zr-Zr pairs include only the Coulomb repulsion from effective charges. The EME-SNAP gives the same trend in forces for each pair, but they are slightly different from the Morse-BKS potentials, as expected. The metal-metal pairs in amorphous oxides are connected through oxygen atoms, and their pair distances are longer than 3 Å. The slightly different two-body pair forces and many-body contributions in SNAP beneficially affect the Ta-Ta, Ta-Zr, and Zr-Zr RDFs beyond 3 Å, which is noted in the following subsection. The DFT O-O and metal-metal pair forces in the calculations only consider the interactions between a single type of element, different from pair forces of the Morse-BKS potentials and EME-SNAP for amorphous oxides.

We also compared cohesive energies E_c of amorphous 50% ZrO_2-doped Ta_2O_5 models computed by various potentials. The cohesive energy from DFT is computed as

$$E_c = \frac{[E_{\text{total}} - N_{\text{Ta}}E_{\text{Ta}} - N_{\text{Zr}}E_{\text{Zr}} - N_{\text{O}}E_{\text{O}}]}{N_{\text{total}}}, \tag{8}$$

where N_x and E_x are the number and the energy of element x, and N_{total} and E_{total} are the total number of atoms and total energy of the system in the unit cell.

Figure 3 shows cohesive energies computed from Morse-BKS and from EME-SNAP potentials on the vertical axis vs DFT cohesive energies on the horizontal axis. Each point in the plot represents one structural model. Two sets of models are investigated, one generated by RMC (square symbols, blue and red) and the other (cross symbols, purple and orange) from RMC models further relaxed using DFT energy minimization. The black dotted line is where the calculated cohesive energy matches perfectly the DFT energy. From the results, we find that the calculated cohesive energies from EME-SNAP are closer to the dotted lines compared to Morse-BKS for both RMC- and DFT-relaxed models. Deviations of EME-SNAP from DFT energies are around 0.05 eV, and of Morse-BKS are around 0.25 eV. The EME-SNAP behaviors as lines parallel to the black dotted line, means the energy differences between models have even lower errors besides the total energy shift, which are more important in the MD simulations.

C. Radial distribution function

In order to get a better idea about the amorphous atomic structures, we calculate partial RDFs for models from DFT, EME-SNAP, and Morse-BKS potentials. The calculated partial RDFs in Fig. 4 are from two sets of models with different numbers of atoms. One set comes from models with 975 atoms (solid lines) that are initially generated by fitting to the experimental x-ray GIPDF using the RMC method [14], and the other comes from models with 19 500 atoms (dotted lines) starting from randomly generated structures based on the experimental measured density followed by heating up and cooling down from 3000 K with the NVT ensemble. The black lines are the references, which represent the atomic structures starting from RMC models and relaxed with DFT energy minimization. From previous work, we find the RMC models are slightly different from the DFT models after energy minimization [12,14]. EME-SNAP is generated based on DFT calculations; here, we are only focusing on the comparison between Morse-BKS and EME-SNAP with DFT as a reference. The red and blue lines represent configurations collected from MD trajectories generated at 300 K in the isothermal isobaric ensemble (NPT) based on the Morse-BKS potentials and EME-SNAP, respectively. Their initial atomic structures are also from the same RMC models. Here, due to the extremely long DFT calculation time for models with 975 atoms, we use DFT-relaxed structures as references instead of configurations from room-temperature MD trajectories. From the results, we find that the partial RDFs from the EME-SNAP models with 975 atoms (red solid lines) match the DFT results (black solid lines) fairly well through the whole range. Meanwhile, the partial RDFs from models with 975 atoms generated from the Morse-BKS potentials (blue solid lines) also have good agreement with the DFT partial RDFs, except for slightly underestimating the first peaks of Ta-Ta, Zr-Zr, and Ta-Zr pairs. The partial RDFs from the 975-atom models are in agreement with the DFT results because both the Morse-BKS potentials and EME-SNAP are both good at describing atomic structures near the same initial RMC structures. Figures 4(d) and 4(f) show significant differences in metal-metal partial RDFs from the 19 500 atom models generated from the Morse-BKS potentials (blue dotted lines) and DFT (black solid lines), especially for the first peak of the Ta-Ta and Ta-Zr pairs, whereas EME-SNAP-generated models (red dotted lines) still give similar partial RDFs compared to those from DFT generated models. Since all 19 500 atom models are from random structures and prepared with the same recipe, we assert that the EME-SNAP is more robust and can lead to structures that agree with

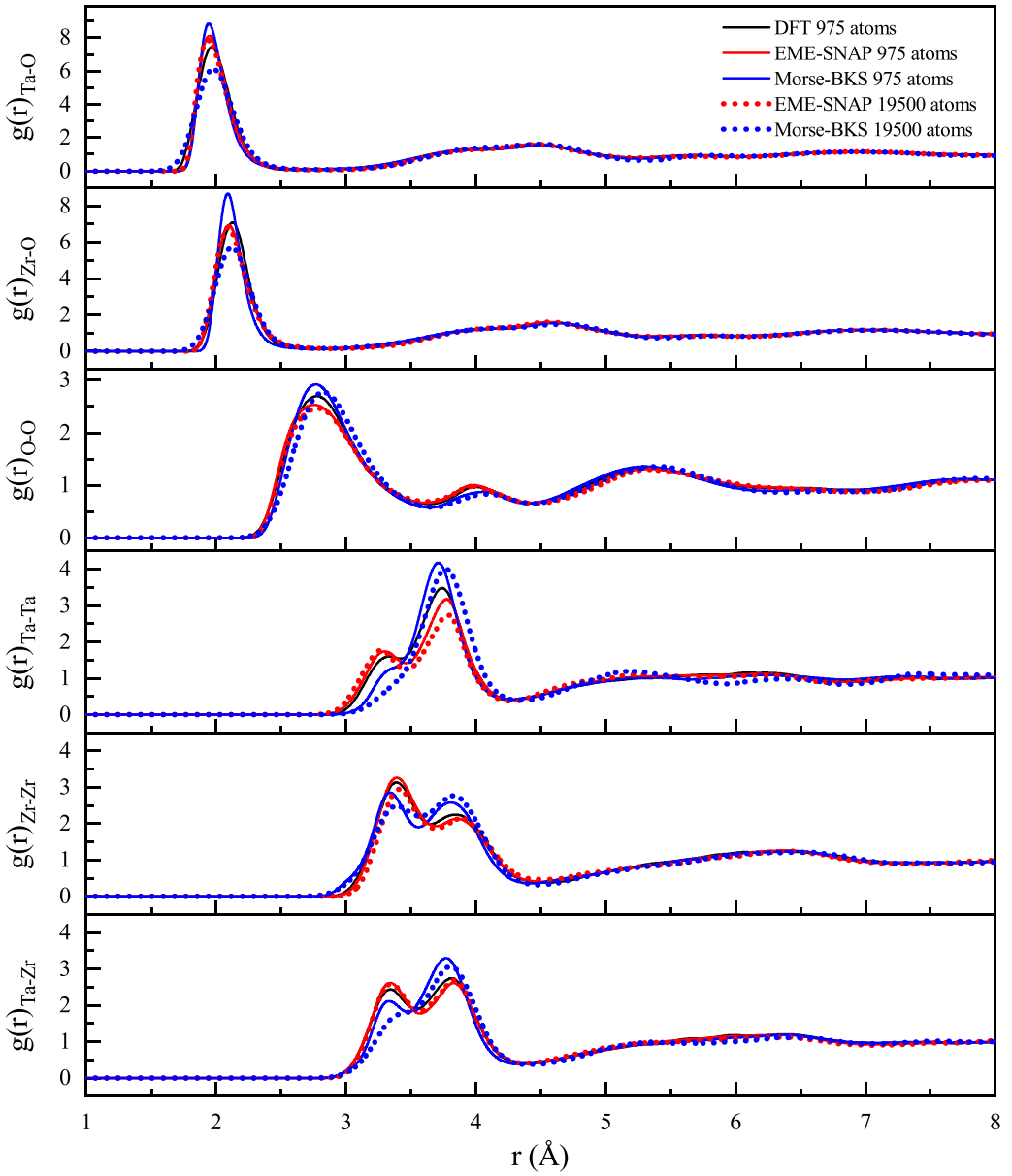

FIG. 4. Radial distribution function comparison of the Morse-BKS potential, the SNAP potential, and DFT results.

partial RDFs from DFT models without the need for RMC fitting.

D. Elastic modulus

The elastic moduli from experimental measurements can be used to verify the quality of the potentials, providing additional information for modeling and simulations. For amorphous materials, calculating elastic moduli with small samples (such as 364-atom models) tend to have significant variations. It is necessary to average over multiple configurations or use a larger model with more atoms to obtain converged results. The calculations with DFT need a huge mount of computational resources, which make it prohibitively expensive. On the other hand, calculations using classical pair potentials and machine learning potentials can easily solve this problem since they can be, at least, 10^3 times faster than DFT.

In this paper, the elastic moduli of amorphous ZrO_2-doped Ta_2O_5 are calculated using models with 19 500 atoms based on the Morse-BKS potentials and EME-SNAP. The elastic moduli are calculated from the elastic strain tensors according to Voigt-Reuss-Hill approximations [38–41]. By changing the simulation box size along different directions, the elastic strain tensors are calculated from the change in the system energies under strain. Compared to the models with 975 atoms or 364 atoms, the larger models (19 500 atoms) the elastic tensors are more isotropic in different directions, and the calculations of the elastic moduli are more consistent due to the better statistics. Table II contains the elastic properties from the Morse-BKS potentials and EME-SNAP, as well as the experimental measurements. The Morse-BKS potentials tend

TABLE II. Elastic properties of ZrO_2-doped Ta_2O_5 from the Morse-BKS models, the EME-SNAP models, and the experimental measurements.

Zr:Ta_2O_5	Zr (%)	Density (g/cm^3)	Young's (GPa)	Bulk (GPa)	Shear (GPa)	Poisson ratio
EME-SNAP	50	6.4	125	91	49	0.27
Morse-BKS	50	6.8	172	123	68	0.27
MLD 2018 [3]	50.2 ± 0.3		130 ± 2			
UMP 551 [3]	41 ± 3	6.1 ± 0.2	125 ± 2			0.21 ± 0.05
UMP 554 [3]	43 ± 3	5.9 ± 0.2	114 ± 2			0.36 ± 0.03
UMP 678 [3]	47 ± 2	6.6 ± 0.2	111 ± 4			0.28 ± 0.09
UMP 680 [3]	47 ± 2	6.5 ± 0.2	110 ± 4			0.28 ± 0.09
CSU III [3]	54 ± 3	7.1	143 ± 5			0.37 ± 0.05

to overestimate Young's modulus, whereas the EME-SNAP results agree well with experiments [3].

E. Simulated annealing with MD simulation

The experimental estimated density of amorphous Zirconia-doped Tantala with 50% Zr cation concentrations is about 6.5 g/cm^3 [12]. We use this value as the initial density for the models. The final density of the amorphous models from the Morse-BKS potentials and EME-SNAP are 6.8 and 6.4 g/cm^3, respectively, after having been equilibrated at 300 K with the NPT ensemble. From Table II, we found that there is a nonlinear relationship between density and doping concentration. The experimental densities of the amorphous materials are also dependent on the deposition methods and annealing processes, further complicating the comparison between experiments and models.

We simulate the annealing of 50% Zirconia-doped Tantala with the EME-SNAP by heating and cooling the models at different rates. First, we heat the models at 20 K/ps from 300 K, then cool the snapshots from different temperatures with different rates. All simulations are performed using models with 19 500 atoms, and we take one snapshot every 10 fs. The results are plotted in Fig. 5.

Figure 5 gives the density and temperature of each configuration. From these results, the models cooled with slower rates from higher temperatures had lower energies, and the potential energies and the densities of models after simulated annealing depend on both annealing temperature and cooling rate. The final densities range from 6.2 to 6.4 g/cm^3, which is slightly lower than the targeted experimental value of 6.5 g/cm^3. The experimental atomic density vs the temperature curve during annealing is not available for comparison, but the large variation of the experimental densities of amorphous SiO_2 [5], amorphous Ta_2O_5 [5], and amorphous ZrO_2-doped Ta_2O_5 [3] suggest a nontrivial dependence on the deposition conditions and annealing temperatures.

F. Simulated mechanical spectroscopy

By applying a periodic strain on the simulation box and calculating the stress responses from MD simulations, we can simulate the mechanical spectroscopy [42–44] of the amorphous materials. The strain vs the potential-energy curve can reveal the potential-energy response to the strain, and it can also be used to check the volume stability of the models. Mechanical spectroscopy has been used to extract mechanical loss properties successfully for amorphous tantala [15].

We applied periodic strain with 0.01 amplitude to 50% Zirconia-doped Tantala with both Morse-BKS and EME-SNAP to simulate mechanical spectroscopy (see Fig. 6). Before we collect the results, 50-ns simulations are performed to allow the atomic structures to be further relaxed under strain. We found that both potentials give similar mechanical spectroscopy. As soon as the additional strain is applied, the potential energies go up. Compression strains show larger energy changes compared to tensile strains with the same amplitude. Comparing the results from Morse-BKS and EME-SNAP, we note that Morse-BKS gives larger energy changes and stress responses, which is consistent with results that Morse-BKS gives a larger elastic modulus in Table II.

IV. CONCLUSION AND DISCUSSION

With training from the energies, forces, and stresses from DFT calculations, we generated an EME-SNAP for amorphous Zirconia-doped Tantala. The EME-SNAP faithfully reproduces the energies, forces, and stresses compared to

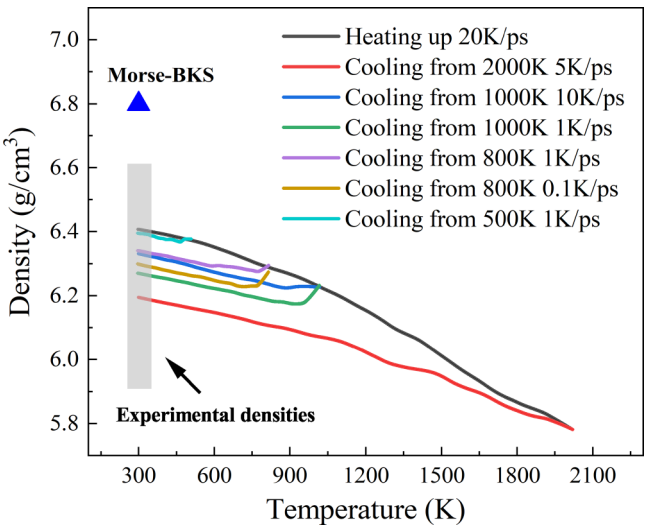

FIG. 5. Temperature vs atomic density of amorphous models during simulated annealing. The blue triangle represents models from Morse-BKS potentials. The gray region is the experiment densities.

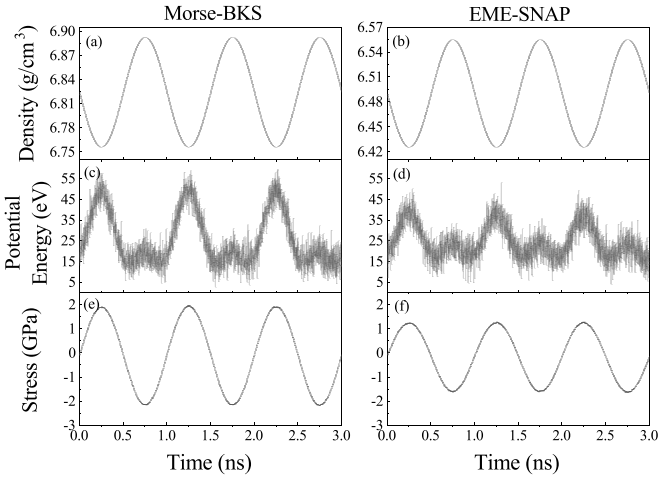

FIG. 6. Mechanical spectroscopy simulations of 50% ZrO_2-doped Ta_2O_5. The frequency of the strain is 1×10^9 Hz at 300 K. (a), (c), and (e) are from models with the Morse-BKS potential, and (b), (d), and (f) are from models with EME-SNAP.

the DFT references. The amorphous Zirconia-doped Tantala models generated from SNAP are able to capture the correct short-range order and better metal-metal partial pair RDFs than the well-built Morse-BKS classical pair potentials. Without any prior knowledge, EME-SNAP is able to learn from training and give a computable potential for the targeted system. The relatively fast calculation speed of EME-SNAP enables large-size models and long-time simulations, which makes more realistic amorphous models with better statistics for properties, such as RDFs and elastic moduli. Doping is also automatically included and becomes a nonissue compared to the classical pair potentials.

Despite the success of the EME-SNAP in this paper, there are still some problems that must be mentioned. In this paper, the EME-SNAP is developed for zirconia-doped amorphous tantala with both crystals and amorphous structures included in the training set, but it cannot capture the recrystallization process when we cool very slowly from high temperatures (> 1000 K). The atoms will have the chance to aggregate together and result in unphysical structures with extremely high potential energies. The higher the temperature is and the slower the cooling rate is, the higher chance the potential fails. This behavior is partially mitigated by using EME-SNAP instead of WD-SNAP, which improves the chemical sensitivity and force accuracy by explicitly considering the partial atomic density for each type of element. Failed structures, DFT MD trajectories at higher temperatures are also added into the training set. They can improve the high-temperature stability, but they also increase errors in the amorphous structures of interest in this paper. Failure in the simulations can also be triggered by the formation of oxygen molecules. Oxygen molecules may exist in real amorphous oxides, and in the two-body force test SNAP shows O-O bonding in oxygen molecules around 1.4 Å. But currently, SNAP does not include them properly, even with liquid oxygen added to the training set. We can avoid this problem by adding an additional repulsive interaction between O atoms, but this modification will increase the training errors significantly and lead to low-density states which are not close to experimental measurements. To avoid these failures, the best approach for now is smoothly mixing 10% to 20% Morse-BKS potentials in the EME-SNAP at high temperatures. Another possible solution is applying the machine learning on-the-fly technique [45,46] to add training structures during simulations and adjust the parameters based on the different atomic environments.

To summarize, the EME-SNAP based on machine learning techniques give us an alternate way of calculating forces and energies with a good balance of accuracy and calculation cost, which enables the modeling of complex systems, such as doped amorphous oxides. With a proper training of the targeted structures, it can be used to study energy landscapesas well as elastic and thermal properties. More effort in improving generality and stability of the potential is required to study more complex physics, such as recrystallization and phase transitions.

ACKNOWLEDGMENTS

This work was supported by the National Science Foundation (NSF) under Awards No. PHY-1707870, No. PHY-2011770, and No. PHY-2011776, and the Gordon and Betty Moore Foundation (GBMF) under Grant No. 6793. Computations were performed using the utilities of the National Energy Research Scientific Computing Center (NERSC) and the University of Florida Research Computing HiPerGator.

[1] N. Kaiser and H. K. Pulker, *Optical Interference Coatings* (Springer, Berlin, 2013), Vol. 88.

[2] J. Aasi, B. Abbott, R. Abbott, T. Abbott, M. Abernathy, K. Ackley, C. Adams, T. Adams, P. Addesso, R. Adhikari *et al.*, Advanced ligo, Class. Quantum Grav. **32**, 115012 (2015).

[3] M. Abernathy, A. Amato, A. Ananyeva, S. Angelova, B. Baloukas, R. Bassiri, G. Billingsley, R. Birney, G. Cagnoli, M. Canepa, M. Coulon, J. Degallaix, A. D. Michele, M. A. Fazio, M. M. Fejer, D. Forest, C. Gier, M. Granata, A. M. Gretarsson, E. M. Gretarsson, E. Gustafson, E. J. Hough, M. Irving, É. Lalande, C. Lévesque, A. W. Lussier, A. Markosyan, I. W. Martin, L. Martinu, B. Maynard, C. S. Menoni, C. Michel, P. G. Murray, C. Osthelder, S. Penn, L. Pinard, K. Prasai, S. Reid, R. Robie, S. Rowan, B. Sassolas, F. Schiettekatte, R. Shink, S. Tait, J. Teillon, G. Vajente, M. Ward, and L. Yang, Exploration of co-sputtered Ta_2O_5–ZrO_2 thin films for gravitational-wave detectors, Class. Quantum Grav. **38**, 195021 (2021).

[4] G. Scannell, A. Koike, and L. Huang, Structure and thermomechanical response of $TiO_2 - SiO_2$ glasses to temperature, J. Non-Cryst. Solids **447**, 238 (2016).

[5] M. Granata, A. Amato, L. Balzarini, M. Canepa, J. Degallaix, D. Forest, V. Dolique, L. Mereni, C. Michel, L. Pinard *et al.*, Amorphous optical coatings of present gravitational-wave interferometers, Class. Quantum Grav. **37**, 095004 (2020).

[6] M. J. Toplis, Density of amorphous oxides, Encyclopedia of Glass Science, Technology, History, and Culture **1**, 301 (2021).

[7] A. Pandey, P. Biswas, and D. A. Drabold, Force-enhanced atomic refinement: Structural modeling with interatomic forces in a reverse monte carlo approach applied to amorphous Si and SiO_2, Phys. Rev. B **92**, 155205 (2015).

[8] B. W. H. van Beest, G. J. Kramer, and R. A. van Santen, Force Fields for Silicas and Aluminophosphates Based on *ab initio* Calculations, Phys. Rev. Lett. **64**, 1955 (1990).

[9] J. Yu, R. Devanathan, and W. J. Weber, Unified interatomic potential for zircon, zirconia and silica systems, J. Mater. Chem. **19**, 3923 (2009).

[10] J. Trinastic, R. Hamdan, Y. Wu, L. Zhang, and H.-P. Cheng, Unified interatomic potential and energy barrier distributions for amorphous oxides, J. Chem. Phys. **139**, 154506 (2013).

[11] J. P. Trinastic, R. Hamdan, C. Billman, and H.-P. Cheng, Molecular dynamics modeling of mechanical loss in amorphous tantala and titania-doped tantala, Phys. Rev. B **93**, 014105 (2016).

[12] K. Prasai, J. Jiang, A. Mishkin, B. Shyam, S. Angelova, R. Birney, D. A. Drabold, M. Fazio, E. K. Gustafson, G. Harry, S. Hoback, J. Hough, C. Lévesque, I. MacLaren, A. Markosyan, I. W. Martin, C. S. Menoni, P. G. Murray, S. Penn, S. Reid, R. Robie, S. Rowan, F. Schiettekatte, R. Shink, A. Turner, G. Vajente, H.-P. Cheng, M. M. Fejer, A. Mehta, and R. Bassiri, High Precision Detection of Change in Intermediate Range Order of Amorphous Zirconia-Doped Tantala Thin Films Due to Annealing, Phys. Rev. Lett. **123**, 045501 (2019).

[13] G. Vajente, L. Yang, A. Davenport, M. Fazio, A. Ananyeva, L. Zhang, G. Billingsley, K. Prasai, A. Markosyan, R. Bassiri *et al.*, Low Mechanical Loss TiO_2 : GeO_2 Coatings for Reduced Thermal Noise in Gravitational Wave Interferometers, Phys. Rev. Lett. **127**, 071101 (2021).

[14] J. Jiang, A. S. Mishkin, K. Prasai, R. Zhang, M. Yazback, R. Bassiri, M. M. Fejer, and H.-P. Cheng, Analysis of two-level systems and mechanical loss in amorphous ZrO_2-doped Ta_2O_5 by non-cage-breaking and cage-breaking transitions, J. Chem. Phys. **154**, 174502 (2021).

[15] F. Puosi, F. Fidecaro, S. Capaccioli, D. Pisignano, and D. Leporini, In silico broadband mechanical spectroscopy of amorphous tantala, Phys. Rev. Res. **1**, 033121 (2019).

[16] R. D. Oeffner and S. R. Elliott, Interatomic potential for germanium dioxide empirically fitted to an *ab initio* energy surface, Phys. Rev. B **58**, 14791 (1998).

[17] G. Gutiérrez and J. Rogan, Structure of liquid GeO_2 from a computer simulation model, Phys. Rev. E **69**, 031201 (2004).

[18] V. Van Hoang, Static and dynamic properties of simulated liquid and amorphous GeO_2, J. Phys.: Condens. Matter **18**, 777 (2006).

[19] M. Micoulaut, Y. Guissani, and B. Guillot, Simulated structural and thermal properties of glassy and liquid germania, Phys. Rev. E **73**, 031504 (2006).

[20] P. S. Salmon, A. C. Barnes, R. A. Martin, and G. J. Cuello, Structure of glassy GeO_2, J. Phys.: Condens. Matter **19**, 415110 (2007).

[21] A. P. Bartók, M. C. Payne, R. Kondor, and G. Csányi, Gaussian Approximation Potentials: The Accuracy of Quantum Mechanics, without the Electrons, Phys. Rev. Lett. **104**, 136403 (2010).

[22] V. L. Deringer and G. Csányi, Machine learning based interatomic potential for amorphous carbon, Phys. Rev. B **95**, 094203 (2017).

[23] D. Dragoni, T. D. Daff, G. Csányi, and N. Marzari, Achieving dft accuracy with a machine-learning interatomic potential: Thermomechanics and defects in bcc ferromagnetic iron, Phys. Rev. Mater. **2**, 013808 (2018).

[24] A. P. Thompson, L. P. Swiler, C. R. Trott, S. M. Foiles, and G. J. Tucker, Spectral neighbor analysis method for automated generation of quantum-accurate interatomic potentials, J. Comput. Phys. **285**, 316 (2015).

[25] M. A. Wood and A. P. Thompson, Extending the accuracy of the snap interatomic potential form, J. Chem. Phys. **148**, 241721 (2018).

[26] M. A. Cusentino, M. A. Wood, and A. P. Thompson, Explicit multielement extension of the spectral neighbor analysis potential for chemically complex systems, J. Phys. Chem. A **124**, 5456 (2020).

[27] A. Jain, S. P. Ong, G. Hautier, W. Chen, W. D. Richards, S. Dacek, S. Cholia, D. Gunter, D. Skinner, G. Ceder, and K. A. Persson, The Materials Project: A materials genome approach to accelerating materials innovation, APL Mater. **1**, 011002 (2013).

[28] S. Plimpton, Fast parallel algorithms for short-range molecular dynamics, J. Comput. Phys. **117**, 1 (1995).

[29] G. Kresse and J. Hafner, *Ab initio* molecular dynamics for open-shell transition metals, Phys. Rev. B **48**, 13115 (1993).

[30] G. Kresse and J. Furthmüller, Efficient iterative schemes for *ab initio* total-energy calculations using a plane-wave basis set, Phys. Rev. B **54**, 11169 (1996).

[31] G. Kresse and J. Furthmüller, Efficiency of *ab initio* total energy calculations for metals and semiconductors using a plane-wave basis set, Comput. Mater. Sci. **6**, 15 (1996).

[32] W. Kohn and L. J. Sham, Self-consistent equations including exchange and correlation effects, Phys. Rev. **140**, A1133 (1965).

[33] P. E. Blöchl, Projector augmented-wave method, Phys. Rev. B **50**, 17953 (1994).

[34] G. Kresse and D. Joubert, From ultrasoft pseudopotentials to the projector augmented-wave method, Phys. Rev. B **59**, 1758 (1999).

[35] J. P. Perdew, K. Burke, and M. Ernzerhof, Generalized Gradient Approximation Made Simple, Phys. Rev. Lett. **77**, 3865 (1996).

[36] J. D. Pack and H. J. Monkhorst, Special points for brillouin-zone integrations–a reply, Phys. Rev. B **16**, 1748 (1977).

[37] A. P. Thompson, Fitsnap3, (2021), https://github.com/FitSNAP/FitSNAP.

[38] D. Chung and W. Buessem, The Voigt-Reuss-Hill (VRH) approximation and the elastic moduli of polycrystalline ZnO,TiO_2 (rutile), and α-Al_2O_3, J. Appl. Phys. **39**, 2777 (1968).

[39] J. R. Ray and A. Rahman, Statistical ensembles and molecular dynamics studies of anisotropic solids, J. Chem. Phys. **80**, 4423 (1984).

[40] W. Shinoda, M. Shiga, and M. Mikami, Rapid estimation of elastic constants by molecular dynamics simulation under constant stress, Phys. Rev. B **69**, 134103 (2004).

[41] G. Clavier, N. Desbiens, E. Bourasseau, V. Lachet, N. Brusselle-Dupend, and B. Rousseau, Computation of elastic constants of solids using molecular simulation: Comparison of constant volume and constant pressure ensemble methods, Mol. Simul. **43**, 1413 (2017).

[42] E. E. Holly, S. K. Venkataraman, F. Chambon, and H. H. Winter, Fourier transform mechanical spectroscopy of

viscoelastic materials with transient structure, J. Non-Newtonian Fluid Mech. **27**, 17 (1988).

[43] L. B. Magalas, Mechanical spectroscopy–fundamentals, in *Solid State Phenomena* (Trans Tech. Publ., Stafa-Zurich, Switzerland, 2003), Vol. 89, pp. 1.

[44] J. Qiao, J.-M. Pelletier, and R. Casalini, Relaxation of bulk metallic glasses studied by mechanical spectroscopy, J. Phys. Chem. B **117**, 13658 (2013).

[45] A. G. Kusne, T. Gao, A. Mehta, L. Ke, M. C. Nguyen, K.-M. Ho, V. Antropov, C.-Z. Wang, M. J. Kramer, C. Long *et al.*, On-the-fly machine-learning for high-throughput experiments: Search for rare-earth-free permanent magnets, Sci. Rep. **4**, 6367 (2014).

[46] Z. Li, J. R. Kermode, and A. De Vita, Molecular Dynamics with On-the-Fly Machine Learning of Quantum-Mechanical Forces, Phys. Rev. Lett. **114**, 096405 (2015).